Materials Advances

ROYAL SOCIETY OF CHEMISTRY

PAPER

View Article Online
View Journal | View Issue

Cite this: *Mater. Adv.*, 2023, 4, 134

Facile synthesis of dual-morphological $MgCo_2O_4$ with remarkable performance for pseudosupercapacitors†

Hang Ni, Zunjie Ke, Tanwei Hu, Wanneng Liu, Yu Tian, * Xiaolong Zhu and Guang Zheng

The facile preparation of electrode materials with superior capacitance can be rationally regarded as a fast and efficient strategy to improve the electrochemical properties of supercapacitors. In this work, dual-morphological $MgCo_2O_4$ (DMCO) was successfully synthesized on Ni foam (NF) through a simple hydrothermal route. Honeycomb-like and urchin-like $MgCo_2O_4$ was clearly observed by scanning electron microscopy (SEM) characterization of DMCO, which exhibited an excellent specific surface area of 100.62 $m^2\ g^{-1}$. The as-prepared DMCO was tested in 2 M KOH electrolyte solution using a standard three-electrode system, and the results showed that DMCO exhibited a superior specific capacitance of 1552.34 F g^{-1} at the current density of 1 A g^{-1}. After 5500 cycles under the condition of 15 A g^{-1}, 110% of the initial capacitance was retained when it is used as a binder-free electrode material for supercapacitors. Additionally, a DMCO//AC asymmetric supercapacitor (DMCO//AC ASC) was assembled with DMCO as the binder-free positive electrode and active carbon (AC) as the negative electrode, which displayed a high energy density of 27.46 W h kg^{-1} at a power density of 825.9 W kg^{-1}, and a yellow light-emitting diode could remain lit for 24 min. The cycling performance of DMCO//AC ASC was investigated at the current density of 8 A g^{-1}, where 98.8% of its initial capacitance was retained after 11 000 cycles, which undoubtedly demonstrates its outstanding and prolonged cycle stability. These remarkable electrochemical performances strongly verify that DMCO possesses great potential as a promising material for energy storage.

Received 6th September 2022,
Accepted 30th October 2022

DOI: 10.1039/d2ma00889k

rsc.li/materials-advances

1. Introduction

With the fast development of the global economy, energy sources are severely being depleted, and traditional energy storage devices cannot satisfy the present development trend due to their distinct disadvantages, and hence they should be replaced by sustainable and green energy storage devices.[1–4] To date, enormous progress has been achieved in the search for potential devices. Nowadays, supercapacitors, also called electrochemical capacitors,[5] are a new type of green energy storage device with the features of conventional capacitors and batteries, which can perfectly satisfy the demand for storing energy. They not only possess a higher energy density than conventional capacitors and higher power density than batteries,[5,6] but have numerous attractive advantages of small size, fast charge–discharge rate, high safety, long lifespan, and high efficiency.[6–10] According to these novel merits, supercapacitors are widely used in daily life, such as small-size electric vehicles.[11] Based on the mechanism of charge storage, supercapacitors can be classified into two types, namely electrostatic double-layer capacitors and pseudo-capacitors (also known as faradaic pseudo-capacitors).[5,12–15] In terms of electrostatic double-layer capacitors, their capacitance mainly comes from the separation of electric charge at the interface between the electrode and electrolyte, whereas the capacitance of faradaic pseudo-capacitors is created by the high-reversible faradaic redox reaction at the electrode surface.[5,16–19] Carbon-based materials such as carbon nanotubes[20,21] and graphene[22] have been frequently used as electrodes for electrostatic double-layer capacitors because they have a high specific area and electrical conductivity. Moreover, metal oxides are always used as the electrodes for faradaic pseudocapacitors given that they are redox-active materials. A reversible faradaic process will occur when metal oxides contact the electrolyte in alkaline solution, which offer a higher capacitance than electrostatic double-layer capacitors. Therefore, it is worthwhile to develop electrode materials for pseudocapacitors.

Key Laboratory of Optoelectronic Chemical Materials and Devices of Ministry Education, Jianghan University, Wuhan 430056, Hubei, People's Republic of China. E-mail: ytian@jhun.edu.cn

† Electronic supplementary information (ESI) available. See DOI: https://doi.org/10.1039/d2ma00889k

Metal oxides include single[8,11,23,24] and ternary transition metal oxides,[1,2,25–28] where ternary transition metal oxides not only have multiple oxidation states but have diverse benefits such as low toxicity and low cost.[5] Moreover, they can provide better electrochemical performances than single transition metal oxides, and thus they are more suitable as the electrode materials of faradaic pseudocapacitors. Among them, cobalt-based transition metal oxides (MCo_2O_4, where M = Mg, Cu, Ni, Zn, Mn, Fe, *etc.*) are representative materials because of their high capacitance. $MgCo_2O_4$ has a theoretical specific capacitance of 3122 F g^{-1}, which is higher than that of other cobalt-based transition metal oxides, such as $NiCo_2O_4$ (2682 F g^{-1}), $CuCo_2O_4$ (2620 F g^{-1}), and $ZnCo_2O_4$ (2604 F g^{-1}),[5,29,30] making it the best candidate for faradaic pseudocapacitors. Although a series of $MgCo_2O_4$ materials has been reported in recent years, the as-synthesized $MgCo_2O_4$ shows a low specific capacitance. Haiwei Gao *et al.* reported the preparation of an $MgCo_2O_4$@ppy composite *via* a two-step method, and the specific capacitance of this composite was 1079.6 F g^{-1} at a current density of 1 A g^{-1}.[5] The specific capacitance of $MgCo_2O_4$ twinned-hemispheres was 626.5 F g^{-1} at a current density of 1 A g^{-1},[31] while the specific capacitance of flower-like $MgCo_2O_4$ was 749.2 F g^{-1} under the condition of 1 A g^{-1}.[32] Huiyu Chen *et al.* reported the synthesis of an $MgCo_2O_4$ nanoflake electrode material with a specific capacitance of 734.1 F g^{-1} at 1 A g^{-1}.[33] Generally, a low specific capacitance is caused by a small specific area, porous structure, poor conductivity, high resistance, poor redox-active sites, and use of binder reagents, resulting in mass powder accumulation in the traditional preparation process. Hence, it is our goal to effectively solve these complex problems and improve the specific capacitance. To overcome these flaws perfectly, Yifeng Teng *et al.* prepared $MgCo_2O_4$ nanosheets directly grown on NF *via* the hydrothermal route using ethanol, and consequently these $MgCo_2O_4$ nanosheets showed an outstanding specific capacitance of 1706 F g^{-1} under the condition of 1 mA cm^{-1}.[34] Yanan Meng *et al.* fabricated a $ZnCo_2O_4$@$NiMoO_4$ composite on NF, possessing a superior specific capacitance of 2316 F g^{-1} under the current density of 10 mA cm^{-1}.[35]

Greatly inspired by the above-mentioned experiments, $MgCo_2O_4$ with two distinct morphologies (honeycomb-like $MgCo_2O_4$ and urchin-like $MgCo_2O_4$) grown on NF was successfully prepared, where the dual morphologies possess the merits of accessible surface area and substantial mesopores, resulting in an excellent electrochemical performance. In addition, the as-assembled asymmetric supercapacitor showed high potential as an energy storage device.

2. Experimental

2.1. Materials and methods

The six main chemical reagents including magnesium nitrate hexahydrate ($Mg(NO_3)_2{\cdot}6H_2O$), cobalt nitrate hexahydrate ($Co(NO_3)_2{\cdot}6H_2O$), urea ($CO(NH_2)_2$), ammonium fluoride (NH_4F), potassium hydroxide (KOH), and AC were purchased from Sinopharm Chemical Reagent Co., Ltd (China). All chemical reagents were of analytical grade and used as received without further purification. DMCO grown on 3D NF was fabricated *via* a simple hydrothermal method. The NF (2 cm × 3 cm) was ultrasonicated and treated with 3 M HCl solution for 15 min to remove NiO on its surface, and subsequently with acetone, ethanol and de-ionized (DI) water for 15 min respectively, and then dried at 40 °C in an oven. In a typical synthesis, 3 mmol $Mg(NO_3)_2{\cdot}6H_2O$, 6 mmol $Co(NO_3)_2{\cdot}6H_2O$, 30 mmol $CO(NH_2)_2$ and 10 mmol NH_4F were dissolved in 70 mL of deionized (DI) water and stirred for at least 1 h to form a pink solution. This solution, coupled with the clear NF, was transferred to a 25 mL Teflon-lined stainless steel autoclave. The autoclave was sealed and heated to 120 °C for 10 h. After it was cooled to room temperature, the sample was taken out and washed many times with DI water and ethanol, respectively. Next, the sample was dried at 60 °C for 5 h. Finally, it was annealed *via* chemical vapor deposition (CVD) at 350 °C for 2 h in air at a ramping rate of 5 °C min^{-1}.

2.2. Characterization

The crystal structure of the as-synthesized product was investigated by powder X-ray diffraction (XRD). The morphology and structures of the product were observed *via* field-emission scanning electron microscopy (SEM, SU8000) with an acceleration voltage of 3 kV and high-resolution transmission electron microscopy (HRTEM, JEM 2100F). The composition and oxidation state of the product were investigated using X-ray photoelectron (XPS, Thermo Fisher Scientific K-Alpha).

2.3. Electrochemical test

The electrochemical performance of the obtained product was conducted on a CHI660E electrochemical workstation (made in Shanghai, China) at room temperature using a three-electrode system composed of a working electrode (DMCO), counter electrode (platinum plate), and reference electrode (saturated calomel electrode) in 2 M KOH electrolyte. The mass loading of active material was about 5 mg. The mass loading was equal to the weight of the annealed NF minus pure NF. Cyclic voltammetry (CV) tests were performed at various scan rates from 1 to 10 mV s^{-1} in the potential range of 0–0.55 V. Galvanostatic charge–discharge (GCD) tests were carried out at a current density of 1–15 A g^{-1} in the range of 0–0.5 V. Electrochemical impedance spectroscopy (EIS) was conducted in the frequency range of 0.01 Hz–100 kHz. The specific capacitance (C, F g^{-1}) of the as-synthesized DMCO was calculated using the GCD curve, as follows:

$$C = I\Delta t/m\Delta V \quad (1)$$

where I (A) is the discharge current, Δt (s) is the discharge time, m (g) is the active mass of the working electrode, and I/m (A g^{-1}) is the current density.

2.4. Assembly of an asymmetric supercapacitor

DMCO//AC ASC was assembled with DMCO as the binder-free positive electrode and AC as the negative electrode in 2 M KOH

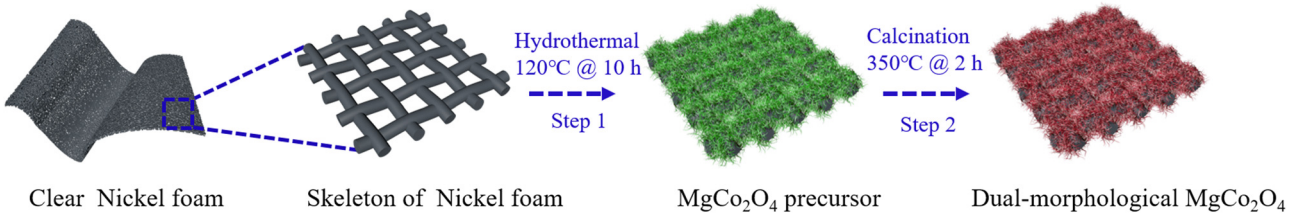

Fig. 1 Schematic illustration of the preparation of the dual-morphological $MgCo_2O_4$.

electrolyte using a two-electrode system. The AC electrode was prepared by mixing AC, acetylene black and polyvinylidene (PVDF) in *N*-methyl pyrrolidone (NMP) with mass ratio of 8 : 1 : 1. The uniform mixed slurry was finally coated on nickel foam and dried at 80 °C for 12 h. To obtain the best mass ratio of positive and negative electrode, the charge balancing theory equation was used, as follows:

$$m_+/m_- = C_-\Delta V_-/C_+\Delta V_+ \quad (2)$$

where m_+ and m_- represent the positive and negative electrode mass, respectively. C_+ and C_- are the specific capacitance of the positive and negative materials, respectively. ΔV_+ and ΔV_- denote the potential range of the positive and negative materials in the three-electrode measurement, respectively. In the case of the DMCO//AC ASC, we found that the best mass ratio was 0.28 according to eqn (2), and consequently the mass loading of the AC electrode was calculated to be around 18 mg and the total mass was around 23 mg. The potential window of the ASC was decided by the current density I/S (where S (cm^2) is the sum of the area of the positive and negative electrodes). The capacitance (C, F g^{-1}), energy density (E, W h kg^{-1}), and power density (P, W kg^{-1}) were calculated based on eqn (1), eqn (3), eqn (4), respectively, as follows:[36]

$$E = C\Delta V^2/7.2 \quad (3)$$

$$P = 3600E/\Delta t \quad (4)$$

where m (g) represents the total mass of the positive and negative materials.

3. Results and discussion

3.1. Morphological and structural characterization

Fig. 1 shows the process for the preparation of the dual-morphological $MgCo_2O_4$. Initially, the NF was treated in a chemical bath for 15 min to remove its oxide layers and impurities, making its surface clear. Subsequently, in the first step, the Mg–Co precursor was formed on the surface of the NF *via* the hydrothermal method (step 1). In the second step, the $MgCo_2O_4$ crystal was formed in an air environment (step 2). Additionally, there was direct contract between the $MgCo_2O_4$ active material and NF, which effectively avoided the use of a conductive and binder agent as in the traditional process, consequently ensuring the utilization of the active material in the electrolyte.

To gain a good understanding of the stability of the NF, its XRD pattern was analysed. Fig. 2a shows photographs of NF, which appeared silvery white before annealing, and then golden yellow after annealing. Subsequently, Fig. 2b exhibits the corresponding XRD patterns, where it can be found that the NF was not greatly different before and after annealing. Undoubtedly, the results suggest that the NF was very stable after annealing.

Fig. 3a shows the XRD pattern of DMCO, confirming its crystal structure and phase purity, where it can be seen that there are 6 main diffraction peaks corresponding to the crystalline planes of (111), (220), (311), (422), (511), and (440) according to the standard card of spinel $MgCo_2O_4$ (JCPDS No. 81-0667). Additionally, no other peaks can be observed, suggesting the high

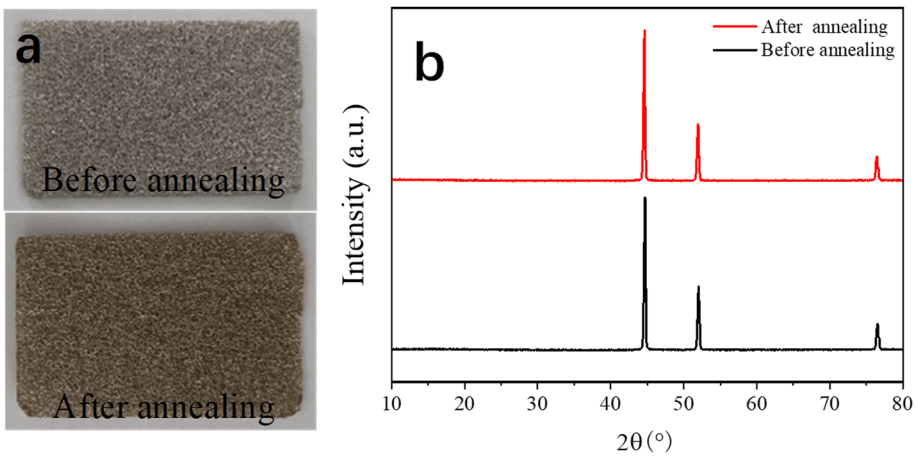

Fig. 2 Photographs (a) and XRD patterns (b) of NF.

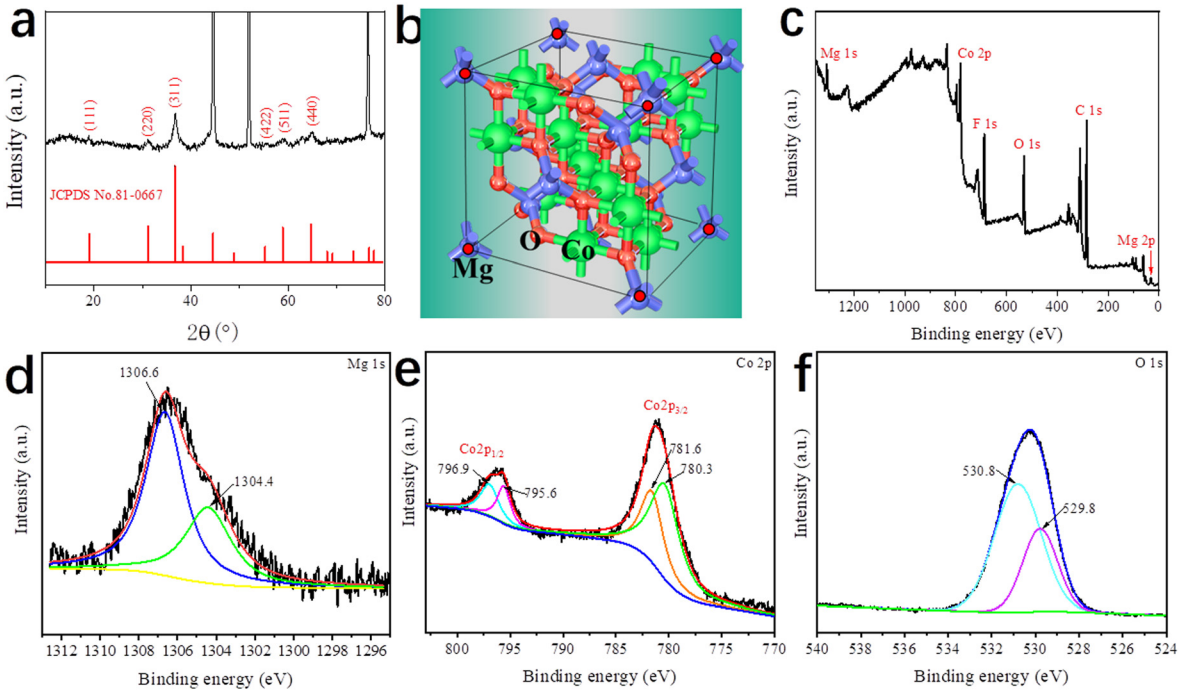

Fig. 3 (a) XRD pattern of DMCO. (b) Unit cell of $MgCo_2O_4$. XPS (c) full survey spectrum, (d) Mg 1s, (e) Co 2p, and (f) O 1s spectra of DMCO.

purity of the as-prepared DMCO. Meanwhile, Fig. 3b shows the unit cell of $MgCo_2O_4$, where the Mg ions occupy the tetrahedral sites and the Co ions occupy the octahedral sites.[34] Fig. 3c–f display the information on the surface chemical element composition and oxidation state of DMCO obtained from the in-depth XPS analysis. Specifically, five elements, *i.e.*, Mg, Co, O, C, and F, appear in the full survey spectrum (Fig. 3c), where the element F comes from the NH_4F in the solution, and the peak of C 1s at 284.8 eV (Fig. 3d) was used to calibrate all the binding energies. In addition, Mg 1s at the binding energy of 1304.4 eV and 1306.6 eV was split into two peaks, which indicates the presence of magnesium oxide.[37,38] The Co 2p spectrum in Fig. 3e exhibits two strong peaks, which correspond to Co $2p_{3/2}$ and Co $2p_{1/2}$ and can be split into four peaks. The fitted peaks at binding energies of 781.6 eV and 796.9 eV are related to Co^{2+}, while the fitted peaks at binding energies of 780. 3 eV and 795.6 eV are related to Co^{3+}, which suggest the coexistence of Co^{2+} and Co^{3+}. The O 1s spectrum is displayed in Fig. 3f, distinctly revealing two peaks at the binding energies of 530.8 eV and 529.8 eV.

To investigate the thermal stability and components of the as-prepared material, thermogravimetric (TG) and derivative TG (DTG) measurements were further performed. Fig. 4 shows the TG and DTG curves of DMCO. The test was carried out from room temperature to 800 °C at a heating ramp of 10 °C min^{-1}. As depicted in Fig. 4, DMCO has a weight loss process with three steps. The first step of weight loss (2.64%) below 200 °C is due to the dehydration (the absorbed water and crystalline water) of the material.[5] The second and third weight loss steps (16.76% and 8.64%) below 387 °C are due to the decomposition of the metal salt.[5] Additionally, distinct peaks appeared at about 208 °C and 350 °C. Meanwhile, no apparent peaks were

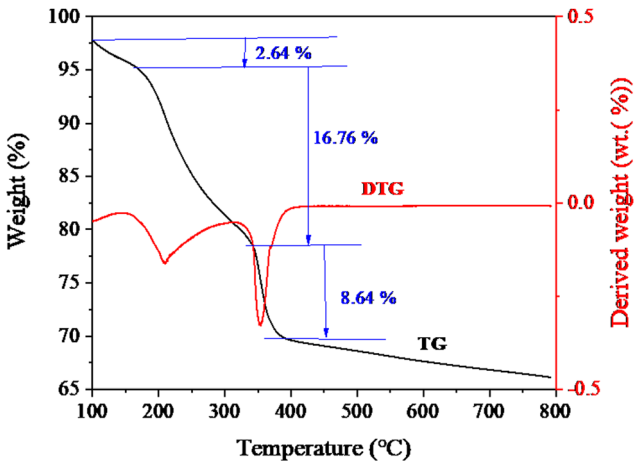

Fig. 4 TG and DTG curves of DMCO.

observed above 350 °C, indicating that material structure was formed and no additional phases existed. Thus, the above-mentioned results prove that DMCO with high purity was synthesized.

The surface morphologies of DMCO were observed by SEM for its physical characterization (Fig. 5a–f). The low- magnification SEM image in the inset of Fig. 5a shows that DMCO possesses the feature of dual morphology (marked as "①" and "②"). According to Fig. 5a (corresponding to "①"), there are plentiful urchin-like $MgCo_2O_4$ whose shapes show a uniform distribution and excellent morphology features. According to the side-magnification SEM image in Fig. 5b, their diameters are about 11 μm. Fig. 5c suggests that the urchin-like $MgCo_2O_4$ is made up of substantial

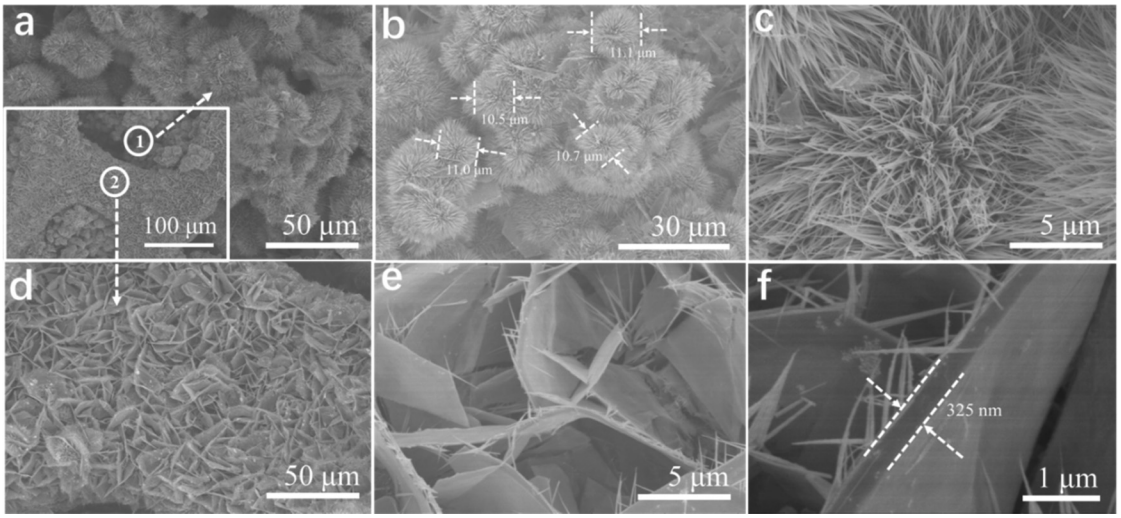

Fig. 5 (a)–(f) SEM images of DMCO at different magnifications.

thin and dense nanowires, which possess the characteristics of different angles and sufficient interval space between nanowires, where a great number of OH^- ions can be filtered and electrons transported for redox reactions according to their overall angle. As shown in Fig. 5d (corresponding to "②"), numerous $MgCo_2O_4$ sheets are densely interwoven to a honeycomb-like structure on the NF, by which numerous pores can be formed, which can fully contact with OH^-, greatly favoring an improvement in electrochemical performance. Fig. 5e shows that the honeycomb-like $MgCo_2O_4$ is composed of sheets on which a small quantity of needle-like $MgCo_2O_4$ grew. Meanwhile, the abundant space between the sheets, which allow the entry of large OH^- ions, increases the access for their surface to contact the alkaline solution when used as an electrode. The high-magnification SEM image in Fig. 5f obviously shows that the thickness of a sheet is about 325 nm. According to SEM, the characteristics of urchin and sheet structures were observed on the electrode, which can be considered a unique morphology, and therefore the value of the electrode is obvious in the electrolyte.

To further explore the microstructure of the as-fabricated DMCO, TEM and high-resolution TEM (HRTEM) were also performed, as important methods for observation. As depicted in Fig. 6a, it can be found that several urchins are interconnected. The TEM image shows that the urchins are comprised of disorderly nanowires interwoven with each other, which is well consistent with Fig. 6e. Furthermore, abundant mesopores were observed on their surface, fully facilitating the transport of ions in the electrolyte. The area marked with a red dotted line in Fig. 6a is enlarged in Fig. 6b, which shows that the nanowires with ultrastructural feature are composed of numerous $MgCo_2O_4$ nanoparticles, and Fig. 6c depicts that the thickness of a nanowire is around 24.44 nm. As shown in Fig. 6d, the HRTEM image exhibits that the interplanar distance of about 0.18 nm can be indexed well to the (331) crystalline planes of $MgCo_2O_4$. As shown in Fig. 6e, a single $MgCo_2O_4$ sheet can be clearly observed and the area with a blue dotted line suggests that needle-like $MgCo_2O_4$ grew on the edge of it, which is consistent with Fig. 5e and f. Fig. 6f is a magnified view of the area with a red dotted line in Fig. 6e, and coupled with Fig. 6g, it can seen that the sheet is also comprised of $MgCo_2O_4$ nanoparticles and possesses several mesopores. This microstructure can absorb substantial OH^- ions in alkaline solution to improve the electrochemical performance. The HRTEM image in Fig. 6h shows the interlayer spacings of 0.20 and 0.28 nm, which are assigned to the (400) and (220) planes of spinel $MgCo_2O_4$. To get in-depth information of the material structure, selected-area electron diffraction (SAED) characterization was performed. As exhibited in Fig. 6i and j, the diffraction rings are very clear, which suggests that DMCO possesses high crystallinity.[34] In addition, though calculation, there are six crystalline planes from the urchin (Fig. 6i) and sheet (Fig. 6j), corresponding to spinel $MgCo_2O_4$. Thus, the results from the HRTEM and SAED analyses agree well with the XRD results. Fig. 6k and l display the element mapping images of the urchin and sheet, respectively, where the Mg, Co, and O elements show uniform distribution on their surface. Based on this, DMCO has the merits of ultrathin structure and mesopores.

To determine the growth mechanism of DMCO in this work, as shown in Fig. 7a and b, different reaction times were used to observe their surface morphologies. As shown in Fig. 7a, the urchin-like $MgCo_2O_4$ composed of straight and thin nanowires looked undamaged when the reaction time was up to 3 h. Upon close observation, it was apparently found that nanowires varied from straight to bent slightly at 7 h and the urchin-like $MgCo_2O_4$ was made up of numerous dense nanowires with a round feature with the reaction reaching 10 h. In the case of the honeycomb-like $MgCo_2O_4$, it can be seen it was not formed when the reaction time was 3 h, as shown in Fig. 7b. Interestingly, several sheets began to connect with each other (the inset) with a smooth surface and edge, as shown in the enlarged SEM image, at 7 h. Subsequently, the $MgCo_2O_4$ sheets became greatly interpretated to form a honeycomb-like structure (the inset) and the sheets had a smooth surface and edge

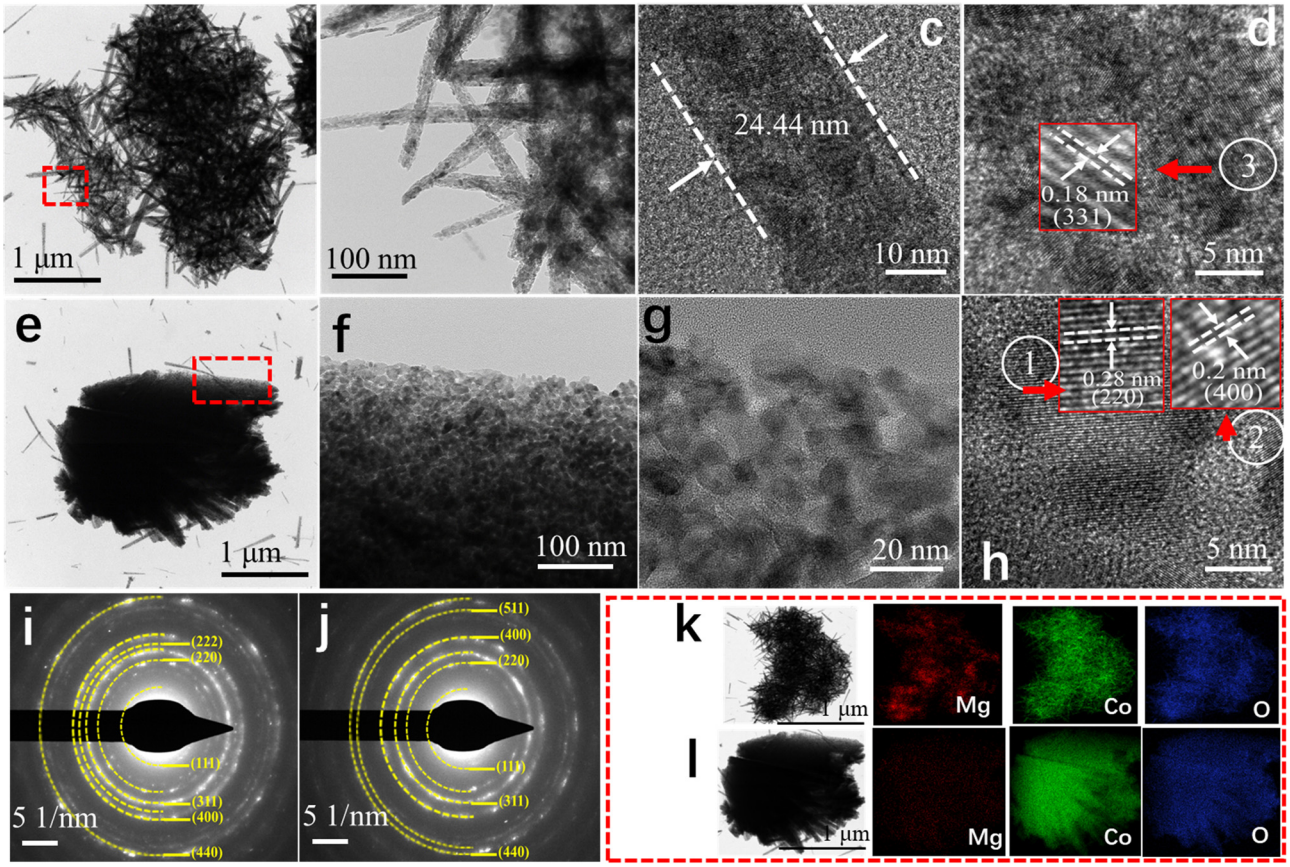

Fig. 6 TEM images of (a)–(c) urchin and (e)–(g) sheet and HRTEM images of (d) urchin and (d) sheet. SAED images of (i) urchin and (j) sheet. Corresponding element mapping images of (k) urchin and (l) sheet.

with needle-like $MgCo_2O_4$ at 10 h, as shown in the enlarged SEM image. Based on the results, it can be seen that the urchin-like $MgCo_2O_4$ has the growth process of "straight → bent slightly → dense", and the honeycomb-like $MgCo_2O_4$ possesses that of "none → several → honeycomb-like". Meanwhile, Fig. 7 also illustrate the growth mechanism.

The BET test plays an indispensable role in analysing the microstructure of materials. Fig. 8 shows the N_2 sorption isotherm and pore size distribution of DMCO. It is obvious that there are hysteresis loops in Fig. 8a ranging from 0.2 to 1.0 P/P_0 and the specific surface area of DMCO in the Fig. 8b exhibits a superior result of 100.62 $m^2\ g^{-1}$, which shows that the urchin-like $MgCo_2O_4$ and honeycomb-like $MgCo_2O_4$ have a significant contribution to the outstanding specific surface area and is superior to that of 63.8[32] and 65.25 $m^2\ g^{-1}$ reported in the literature.[36] Generally, a larger specific surface area indicates that the electrode exposes large accessible electrochemically active sites, where the chemical redox reaction occurrs.[36] With an increase in the number of electrochemical reaction sites, the chemical effect of the reversible redox reaction enhanced between the electrolyte and active materials on the electrode surface. Meanwhile, a large specific surface area can also improve the electrochemical performance by accelerating the insertion and extraction of ions in the electrolyte.[36] The pore size distributions are shown in Fig. 8b. The pore size of DMCO is 6.806 nm, which belongs to the range of mesopores (2–50 nm) and the pore volume of DMCO is 0.221 cc g^{-1}, which far exceeds that of the $NiCo_2O_4$@$MnMoO_4$ composite (0.1372 cc g^{-1}).[36] Therefore, the large specific surface area, substantial mesopores and suitable pore size to absorb large ions are obviously beneficial for enhancing the specific capacitance of the material.

3.2. Electrochemical performance of DMCO

The electrochemical performance of the DMCO electrode material was investigated in 2 M KOH using the standard three-electrode system, including CV, GCD, EIS and cycle performance. Fig. 9a–i show the information from the CV curves of the DMCO electrode, which is an extremely efficient method to observe the electrochemical behavior of the material in the electrolyte. Fig. 9a shows the CV curve of the DMCO electrode at a scan rate of 1 mV s^{-1} in the potential range of 0 to 0.55 V. It can obviously be found that the sharp of CV curve exhibits an irregular rectangular, which means a typical pseudocapacitive characteristic. The redox peak observed in the range of 0–0.55 V originates from the faradaic redox reactions related to *M*–O/*M*–O–O–H with the alkaline electrolyte,[39] where *M* represents Mg or Co ions. The CV curves at different scan rates of 1, 3, 5, and 8 mV s^{-1} are presented in Fig. 9b, where the redox peaks of all the CV curves are distinct. Furthermore, the pair of redox peaks gradually shifts towards the positive

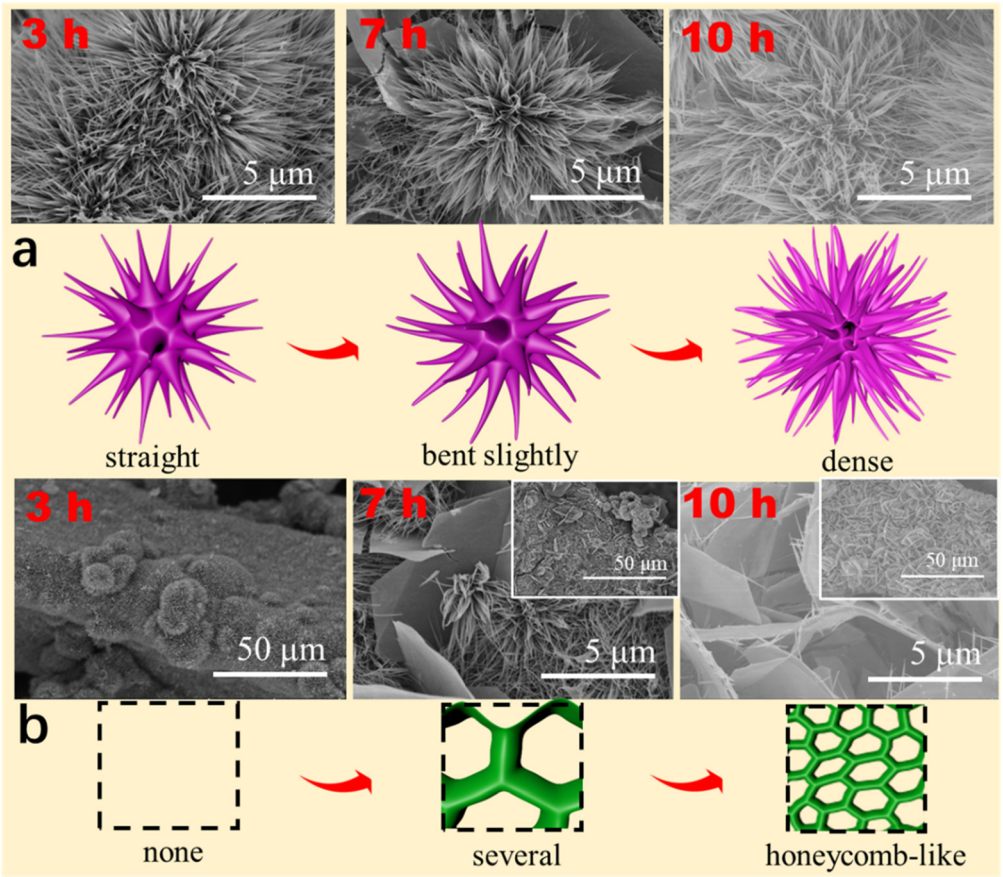

Fig. 7 Growth mechanism of (a) urchin-like $MgCo_2O_4$ and (b) honeycomb-like $MgCo_2O_4$.

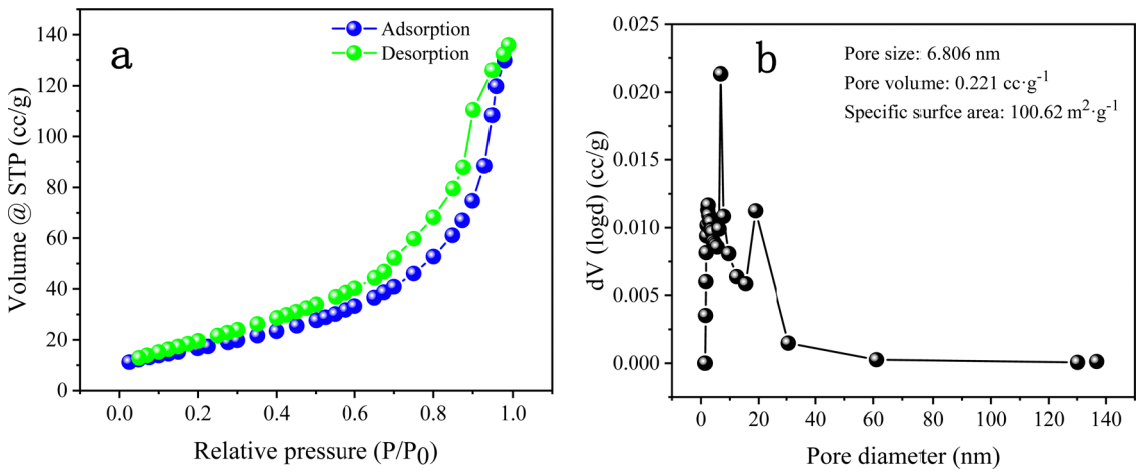

Fig. 8 (a) N_2 adsorption–desorption isotherm and (b) corresponding pore size distributions of DMCO.

potential and negative potential with an increase in the scan rate, leading an increase in the peak currents. This is due to the ohmic resistance and polarization effect in the electrode.[32] Meanwhile, Fig. 9c shows the square root of the scan rate *vs.* cathodic peak current curve, directly reflecting their linear relationship, which suggests that DMCO shows battery-type behavior in KOH solution.[40] Fig. 9d shows the linear relationship between the anodic and cathodic current and scan rate at 0.3 V from the CV test, which suggests that DMCO possesses excellent conductivity.[41] To represent the electrochemical behavior of the DMCO electrode as a specific value, eqn (5) was employed, as follows:

$$i = av^b \quad (5)$$

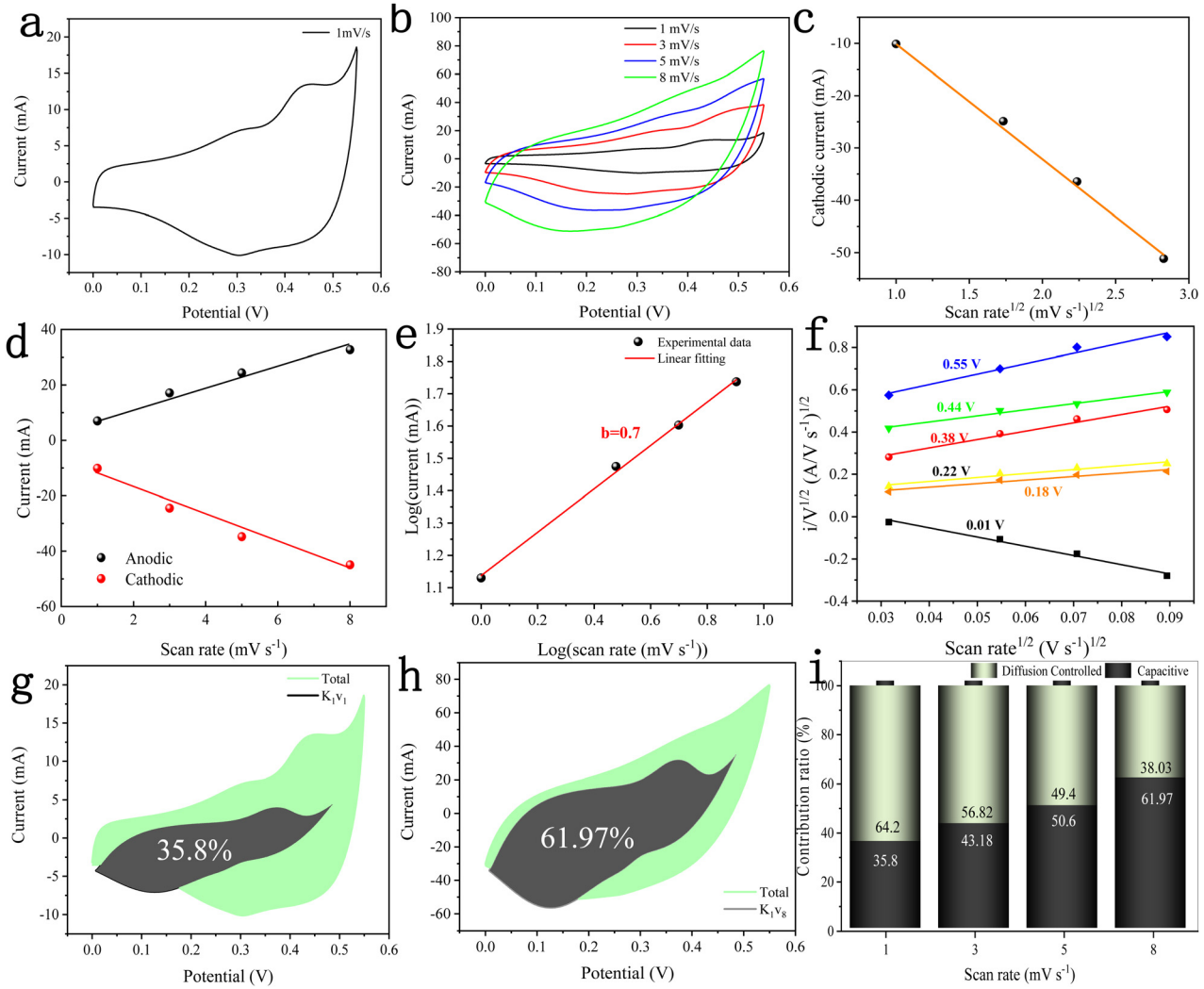

Fig. 9 CV curves (a) at 1 mV s^{-1} and (b) at different scan rate, (c) cathodic peak current *vs.* the square root of the scan rate curve, d) linear relationship between response current and scan rates at 0.3 V, (e) linear relationship between logarithm anodic peak current and logarithm scan rates at 0.45 V, and (f) plots of $i/v^{0.5}$ *vs.* $v^{0.5}$ at different potentials. Capacitive (black area) and diffusion-controlled (green area) contribution at (g) at 1 mV s^{-1} and (h) 8 mV s^{-1}, and (i) capacitive (black area) and diffusion-controlled (green area) contribution ratio at different scan rates of DMCO.

where a represents the response current (mA), v represents the scan rate (mV s^{-1}), and a and b denote constants. Then, eqn (5) can be transformed into eqn (6), as follows:

$$\log i = b \log v + \log a \quad (6)$$

As is known, when the b value is around 0.5, the storage process is mainly a diffusion-controlled process, surface-capacitive and diffusion-controlled processes coexist when the b value ranges from 0.5 to 1 and surface capacitance dominates when the b value is close to 1.[42] As revealed in Fig. 9e, the slope of the anodic current at 0.45 V divided by different scan rate is about 0.7, elaborating that the reactions between DMCO and the electrolyte is caused by both diffusion-controlled and surface-capacitive processes, which is in accordance with the redox peaks in Fig. 9a and b.

To further explore the pseudocapacitive behavior of the DMCO electrode, the CV curves in Fig. 9b were considered. The CV curve usually includes two types of energy storage modes,[43] namely a faradaic process (also called faradaic contribution) arising from redox reactions, and a non-faradaic process (also called non-faradaic contribution) from the electric double layer. The so-called faradaic contribution includes a diffusion-controlled OH^- insertion process and a redox pseudocapacitive process occurring at the surface atoms, even possibly, with atoms located in the interlayer lattice planes of the active materials.[44] Besides, the non-faradaic contribution comes from double-layer capacitance.[44] According to the research by Dunn and co-workers, the contribution from surface pseudocapacitance and double-layer capacitance (capacitive contribution, marked as "cap"), as well as diffusion-controlled OH^- insertion contribution (diffusion-controlled contribution, marked as "diff") can be calculated using the CV curves in Fig. 9b according to the following equation:

$$i(V) = i_{cap} + i_{diff} = k_1 v + k_2 v^{0.5} \quad (7)$$

where i (A), V, k_1 and k_2, and v (V s^{-1}) represent the response current, potential, constants, and scan rate, respectively. Additionally, k_1v and $k_2v^{0.5}$ represent the current caused by capacitive contribution and diffusion-controlled OH^- contribution,[43] respectively. The above-mentioned equation can also become eqn (8), as follows:

$$i(V)/v^{0.5} = k_1v^{0.5} + k_2 \quad (8)$$

only by getting the values of k_1 at different potentials in the range of 0–0.55 V to determine the capacitive contribution. In this work, we took advantage of the four CV curves in Fig. 9b to get k_1, and subsequently, k_1 multiplied by the scan rate is the capacitive contribution of every curve obtained at a particular scan rate. Through calculation, Fig. 9f was finally obtained, which shows approximate straight lines, by plotting $i/v^{0.5}$ *vs.* $v^{0.5}$ at different potentials. The capacitive contribution rate was determined based on the proportion of the two areas in the CV area. In Fig. 9g, the capacitive contribution (marked as black area) to the charge storage in the potential window of 0–0.55 V was found to be 35.8% in comparison with the diffusion-controlled contribution (marked as green area) at a scan rate of 1 mV s^{-1}, while that in Fig. 9h at 8 mV s^{-1} is 61.97% for the DMCO electrode. Different contributions corresponding to the

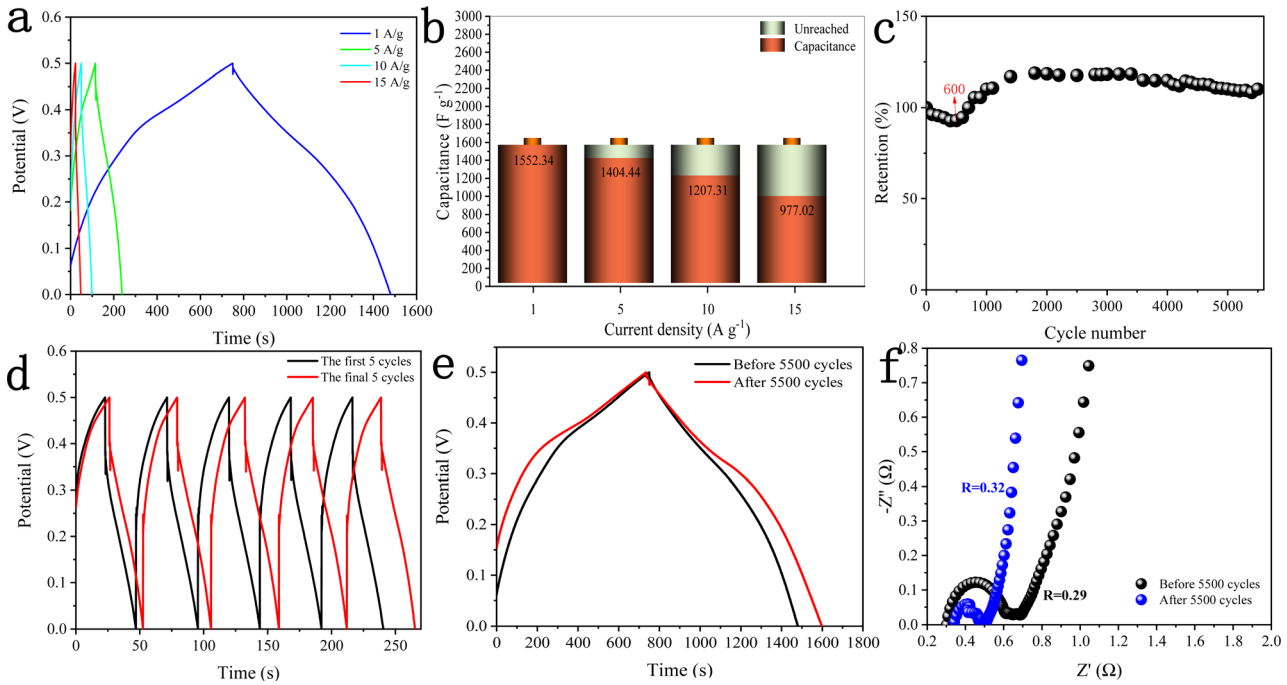

Fig. 10 (a) GCD curves of DMCO at different current densities. (b) Specific capacitance *vs.* current density histogram for DMCO. (c) Cycle performance of DMCO at 15 A g^{-1}. Comparison curves of (d) first and final 5 cycles and (e) at 1 A g^{-1} after cycling, (f) EIS of DMCO before and after cycling.

Table 1 Comparison of the electrochemical properties between DMCO and other $MgCo_2O_4$ materials in earlier reports

Material	Q	Stability	Potential (V)	Ref.
Double-urchin like $MgCo_2O_4$	508 F g^{-1}@2 A g^{-1}	95.9%@2000 cycles	0.5	1
$MgCo_2O_4$@ppy	1079.6 F g^{-1}@1 A g^{-1}	97.4%@1000 cycles	0.45	5
$MgCo_2O_4$@MnO_2	968.98 F g^{-1}@1 mA cm^{-2}	91.45%@5000 cycles	0.5	29
$MgCo_2O_4$@MnO_2	887.3 F g^{-1}@1 A g^{-1}	86.0%@3000 cycles	0.4	30
$MgCo_2O_4$ twinned hemispheres	626.5 F g^{-1}@1 A g^{-1}	68.9%@5000 cycles	0.45	31
Flower-like $MgCo_2O_4$	749.2 F g^{-1}@1 A g^{-1}	67.8%@5000 cycles	0.45	32
$MgCo_2O_4$ nanoflakes	743.1 F g^{-1}@1 A g^{-1}	94.2%@5000 cycles	0.43	33
$MgCo_2O_4$ nanosheet arrays	1706 F g^{-1}@1 mA cm^{-2}	94.65%@3000 cycles	0.5	34
$MgCo_2O_4$ nanosheet arrays	1721.8 F g^{-1}@2 A g^{-1}	96%@5000 cycles	0.55	40
$MgCo_2O_4$@$NiMoO_4$	1775 F g^{-1}@1 A g^{-1}	74.7%@5000 cycles	0.5	49
$MgCo_2O_4$ nanosheets	1431.2 F g^{-1}@1 A g^{-1}	97.65%@10 000 cycles	0.35	50
$MgCo_2O_4$@CoFe	2007 F g^{-1}@1 A g^{-1}	80.2%@5000	0.45	51
$MgCo_2O_4$@NiMn	3757.2 F g^{-1}@1 A g^{-1}	86.9%@5000	0.5	52
$MgCo_2O_4$ nanoflakes	772.7 F g^{-1}@1 A g^{-1}	Not reported	0.55	53
$MgCo_2O_4$ nanowires	638.5 F g^{-1}@1 A g^{-1}	Not reported	0.55	53
$MgCo_2O_4$@NiCo	5701.2 F g^{-1}@1 A g^{-1}	83.7%@5000	0.5	54
DMCO	1552.34 F g^{-1}@1 A g^{-1}	110%@5500 cycles	0.5	This work

scan rates of 1, 3, 5, and 8 mV s^{-1} are fully exhibited in Fig. 9i, and as expected, the capacitive contribution increased, while the diffusion-controlled contribution decreased with an increase in the scan rate. Furthermore, it is well-known that the higher scan rate, the greater capacitive contribution, as was the case in this work, which agrees well with the related literature.[42,44] Thus, the above-mentioned results demonstrate that DMCO is a faradaic-capacitive electrode material with high conductivity.

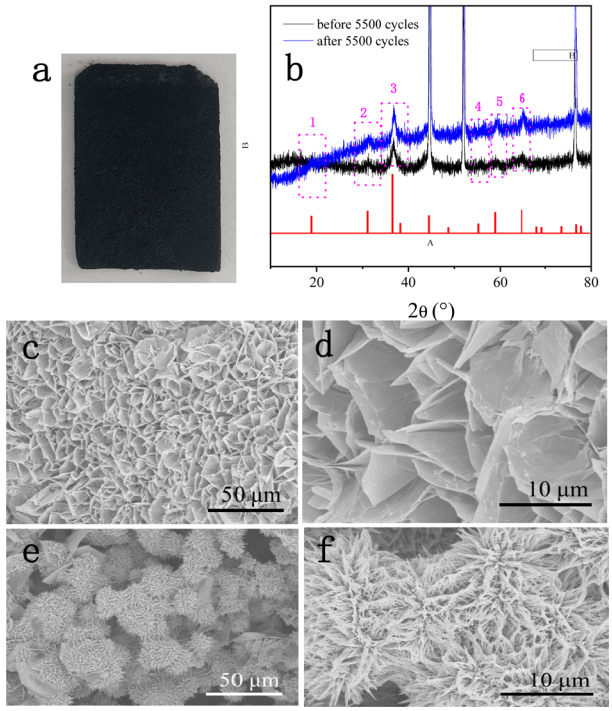

Fig. 11 (a) Photograph of NF after 5500 cycles, (b) XRD patterns before and after 5500 cycles, and SEM images of (c) and (d) honey-comb $MgCo_2O_4$ and (c) and (f) urchin-like $MgCo_2O_4$ after 5500 cycles.

Fig. 10a shows the GCD curves of the DMCO electrode measured at different current densities in the potential window of 0 and 0.5 V, where it can be seen that the charging time of all the GCD curves is basically equal to the discharge time, showing that it exhibits high coulomb efficiency.[45] Besides, all the curves are symmetric, demonstrating its good electrochemical reversibility. The specific capacitance (Cs) of the DMCO electrode was calculated using eqn (1). As shown in Fig. 10b, the DMCO electrode exhibited a specific capacitance of 1552.34, 1404.44, 1207.31, and 977.02 F g^{-1} at the current density of 1, 5, 10, and 15 A g^{-1}, respectively. This notable change is because the smaller current density, the slower the contact between the DMCO active material and OH^-, and thus the higher utilization of the DMCO active material.[46] Cycle stability is a vital measurement for electrode materials used for supercapacitors. Thus, as revealed in Fig. 10c, it can be seen that the capacitance increased at the beginning of the 600th cycle and the cycling test was performed at a current density of 15 A g^{-1} for 5500 cycles. Consequently, it retained 110% of its initial specific capacitance, which indicates its remarkable electrochemical stability. Moreover, Fig. 10d and e show a comparison of the curves between the first and final 5 cycles, as well as at 1 A g^{-1}, where it can be directly seen that they greatly differ, revealing that DMCO has great long-life cyclic stability. To evaluate the internal resistance and diffusion effect of the DMCO electrode, EIS in the frequency range of 0.001–100 kHz for before and after 5500 cycles was performed. The EIS curve is composed of a semicircle in the high frequency region and a straight line in the low frequency region. The diameter of the semicircle is controlled by electrochemical polarization, characterizing the

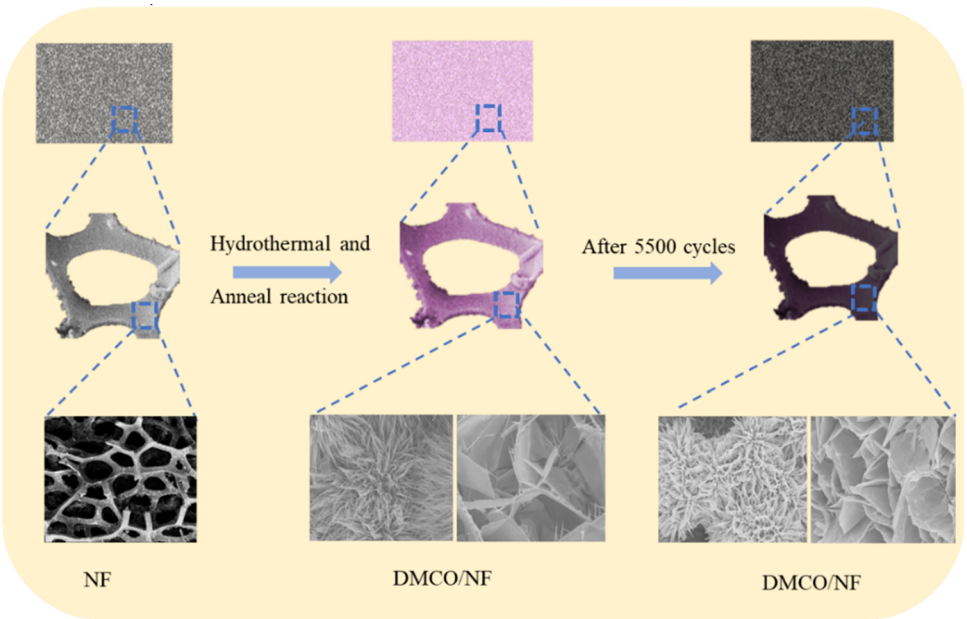

Fig. 12 Schematic illustration of the evolution of DMCO.

faradaic reactions,[47] which corresponds to the charge contact, *i.e.*, the transfer resistance (R_{ct}) between the electrode material and the electrolyte. Specifically, the bigger the semicircle, the larger resistance. The linear slope of a straight line is controlled by physical diffusion, corresponding to the resistance of electrolyte migration in the electrode material (the Warburg resistance), where the larger the linear slope, the smaller the impedance, which is inversely proportional. Besides, the intersection formed by the EIS curve and the real axis Z' reflects the internal resistance (Rs) of the electrode, representing the sum of the ionic resistance of the electrolyte, the intrinsic resistance of the active material and the contact resistance at interface between active material and collector.[47] Fig. 10f presents the EIS curves of DMCO, showing a straight line in the low frequency region, and the inset illustrates a semicircle in the high frequency region, from which DMCO electrode exhibits a low *Rs* of 0.29 and 0.32 Ω before and after 5500 cycles, respectively. In the low frequency region, the two straight lines are parallel to the imaginary axis Z'', revealing the excellent diffusion effect and the capacitive behavior of the electrode.[48] The value of R_{ct} is related to the diameter of the semicircle. For the high frequency region, it can obviously be seen that the diameter after 5500 cycles is smaller than that before, suggesting that the DMCO electrode possesses a relatively low resistance after long-term cycling. Furthermore, the electrochemical performance of DMCO prepared in this work is much more remarkable than that of some relevant reports in the literature, the detailed data of which is presented in Table 1. The detailed data comparison in Table 1 fully shows that the as-fabricated DMCO possesses the feature of excellent electrochemical stability, making it suitable for application in pseudosupercapacitors. Thus, the discussion above suggests that DMCO possesses the characteristic of low resistance and high specific capacitance.

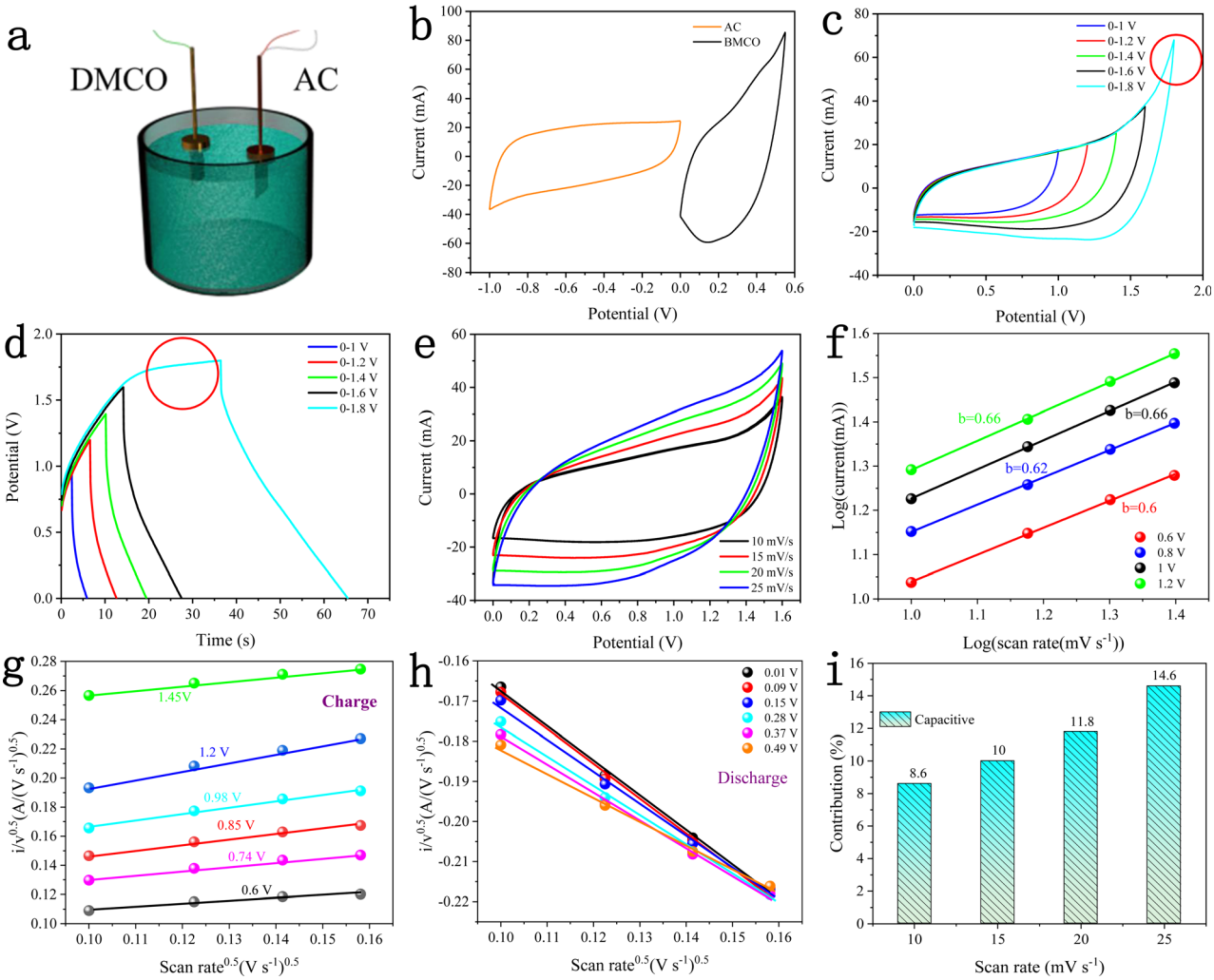

Fig. 13 (a) Schematic illustration of the two-electrode device, (b) CV curves of DMCO electrode and AC electrode measured at a scan rate of 10 mV s^{-1} in the three-electrode system, (c) CV curves at 10 mV s^{-1} and (d) GCD curves at 5.75 mA cm^{-2} of DMCO electrode with different potential windows, and (e) CV curves of DMCO//AC ASC at different scan rates. (f) Linear relationship between logarithm anodic peak current and logarithm scan rates at different potentials for DMCO//AC ASC. Plots of $i/v^{0.5}$ *vs.* $v^{0.5}$ at different potentials for DMCO//AC ASC during (g) charge and (h) discharge. (i) Capacitive contribution ratio of DMCO//AC ASC at different scan rates.

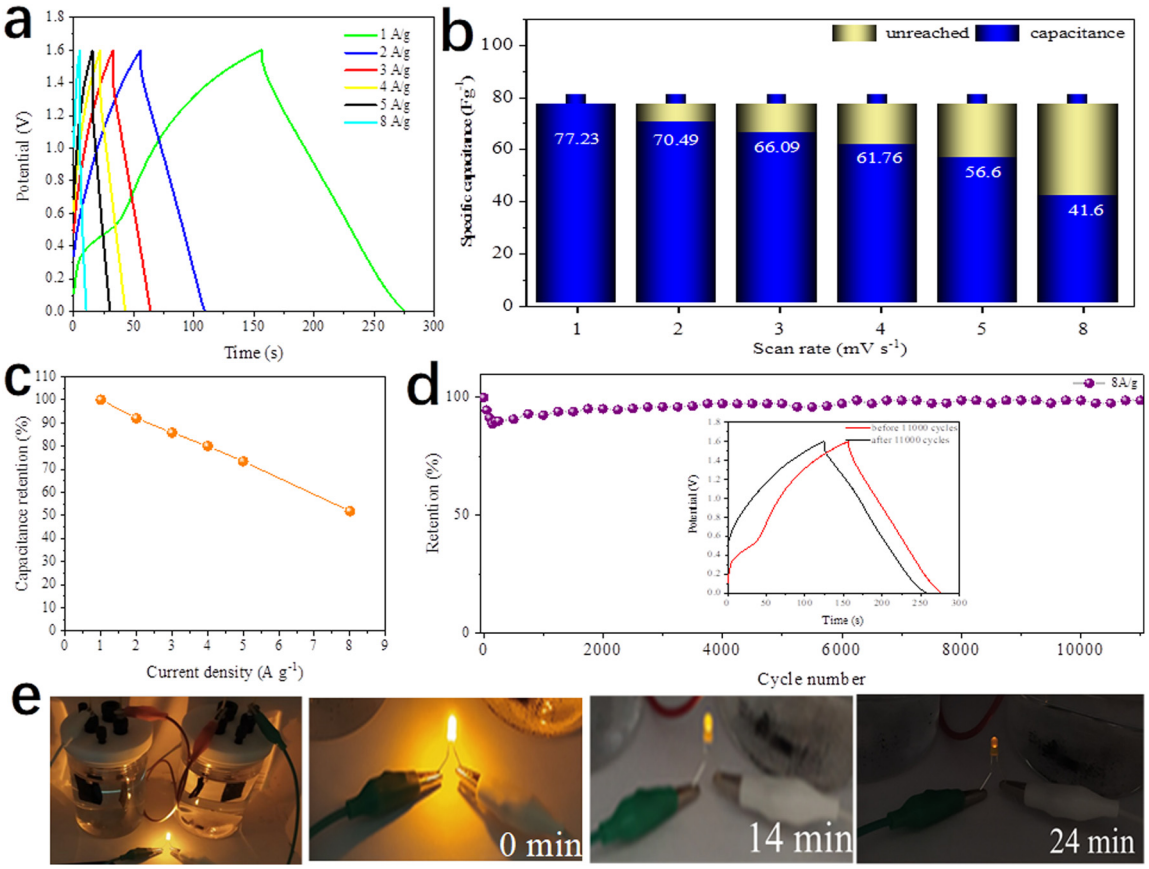

Fig. 14 (a) GCD obtained at various current density, (b) current density *vs.* specific capacitance curve, (c) current density *vs.* capacitance retention, (d) cycle performance at 8 A g^{-1}, and inset shows GCD curves before and after 11 000 cycles at 1A g^{-1}, and (e) application of the DMCO//AC ASC to light a yellow LED and variation in the brightness of the yellow LED.

To gain a further understanding of the stability of DMCO, XRD and SEM were used to investigate its crystal structure and observe its morphologies and structure after prolonged cycling, respectively. Fig. 11a shows a photograph of NF and Fig. 11b reveals the XRD pattern before and after 5500 cycles, where it can seen that the former and the latter barely differ; meanwhile, they possess the same 6 main peaks. The results suggest that the crystal microstructure of DMCO was considerably stable after the long-term durability test. Fig. 11c and e distinctly show that the morphologies of the honeycomb-like $MgCo_2O_4$ and urchin-like $MgCo_2O_4$ remained basically flawless. Fig. 11d and f suggest that the crystal lattice of the honeycomb-like $MgCo_2O_4$ and urchin-like $MgCo_2O_4$ is the same as before, which highlights the outstanding stable performance of DMCO and agrees well with the result in Fig. 10c. Therefore, these results further prove that DMCO can be highly used as an advanced electrode material. Meanwhile, a schematic illustration of the morphological evolution of DMCO is presented in Fig. 12.

3.2. Electrochemical performance of DMCO//AC ASC

To test the practical value and application potential of the DMCO electrode, as shown in Fig. 13a, a two-electrode device was assembled with DMCO and AC as the binder-free positive and negative electrode, respectively, in the electrolyte of 2 M KOH. Fig. 13b displays the CV curves of the AC electrode (−1.0 to 0.0 V) and DMCO electrode (0.0 to 0.5 V) measured at scan rate of 10 mV s^{-1} in a three-electrode system. Fig. 13c shows the CV curves at various potential windows ranging from 0–1.0 V to 0–1.8 V at the scan rate of 10 mV s^{-1}. It is obvious that the stable potential window can be extended by up to 1.6 V, which was also further confirmed by the GCD curves. When the potential window was further increased to 1.8 V, a clear sharp

Table 2 Comparison of the maximum energy density between DMCO//AC ASC and other ASCs

ASC	Maximum energy density	Power density	Ref.
$MgCo_2O_4$ @MnO_2//AC	26.44	289.9	29
$ZnCo_2O_4$@$NiMoO_4$//AC	25.3	787.9	35
$MgCo_2O_4$//AC	12.99	448.7	40
$NiCoSe_2$//AC	24	800	56
$CuCo_2O_4$@$Co(OH)_2$//AG	19.2	350	57
MnO_2@$NiCo_2O_4$/AC	26.6	800	58
$CoSe_2$@$NiSe_2$//AC	20.4	798	59
$NiSe_2$@CNT//AC	25.61	810	60
$NiCo_2O_4$@$MnMoO_4$//AC	15	336	61
DMCO//AC	27.46	825.9	This work

Remark: AG denotes as activated graphene.

peak, as circled in red, was observed, which may be due to the electrolyte degradation/water splitting.[55] Fig. 13d presents the GCD curves varying from 0–1 V to 0–1.8 V at a current density of 5.75 mA cm^{-2}, where the GCD curves in the potential range of 0–1.6 V are greatly symmetric, suggesting that the stable potential window can reach 1.6 V, agreeing well with the CV result. Fig. 13e illustrates the CV curves of the DMCO//AC asymmetric supercapacitor with a 1.6 V potential window at different scan rates. It can obviously be seen that the closed CV curve shows non-rectangular shape, which indicates that electric double-layer capacitance and pseudo-capacitance co-exist. As shown in Fig. 13f, the slopes of the four straight lines composed of different anodic currents are around 0.6, indicating that the reaction in the whole system is determined by diffusion and surface capacitance according to eqn (7). To get more clear information, through calculation using eqn (9), Fig. 13g and h are finally illustrated, where approximate straight lines were obtained by plotting $i/v^{0.5}$ *vs.* $v^{0.5}$ at different potentials during the charge and the discharge. The capacitive contribution rate was determined based on the proportion of two areas in the CV area. Fig. 13i shows that capacitive contribution ratio increased with an increase in the scan rate.

Fig. 14a depicts the GCD curves of the DMCO//AC ASC at various current densities in the potential window from 0 to 1.6 V. The specific capacitance was calculated according to eqn (1). As presented in Fig. 14b, the DMCO//AC ASC exhibited the capacitance of 77.23, 70.49, 66.09, 61.76, 56.6 F g^{-1} and 41.6 F g^{-1} at a current density of 1, 2, 3, 4, 5 A g^{-1} and 8 A g^{-1}, respectively. Besides, the ASC showed 51.8% of its initial specific capacitance at a current density of 8 A g^{-1}, as shown in Fig. 14c, demonstrating that the DMCO//AC ASC can be safely used at a large current density of 8 A g^{-1}.[36] When the current density was 8 A g^{-1}, as shown in Fig. 14d, the DMCO//AC ASC maintained about 98.8% of its initial capacitance after 11 000 cycles, suggesting its remarkable cycle stability. The inset displays the GCD curves before and after 11 000 cycles, where they are similar, which is in agreement with Fig. 14d. Based on eqn (3), (4), and (5), the DMCO//AC ASC has a maximum energy density of 27.46 W h kg^{-1} at a power density of 825.9 W kg^{-1}, and even a maximum power density of 10 240 W kg^{-1} at a power density of 14.79 W h kg^{-1}. Besides, the maximum energy density of the DMCO//AC ASC shows its excellent electrochemical property according to Table 2. It is worthwhile to notice that the cycle stability of the DMCO//AC ASC is much more outstanding compared with other ASCs, as shown in Table 3. Consequently, these results demonstrate that the DMCO//AC ASC can be favorable for energy storage and possesses great potential for practical application. Fig. 14e

Table 3 Comparison of the cycle stability of DMCO//AC ASC and other ASCs

ASC	Cycle stability	Ref.
$MgCo_2O_4$@ppy//AC	91%@10 000 cycles	5
$MgCo_2O_4$@$NiMoO_4$//AC	71.7%@10 000 cycles	49
$NiCo_2O_4$@$MnMoO_4$//AC	96%@10 000 cycles	61
$CuCo_2O_4$@Ni–Co–S//AC	83.6%@8000 cycles	62
$MnCo_2O_4$@OMEP//AC	90.2%@10 000 cycles	63
DMCO//AC	98.8%@11 000 cycles	This work

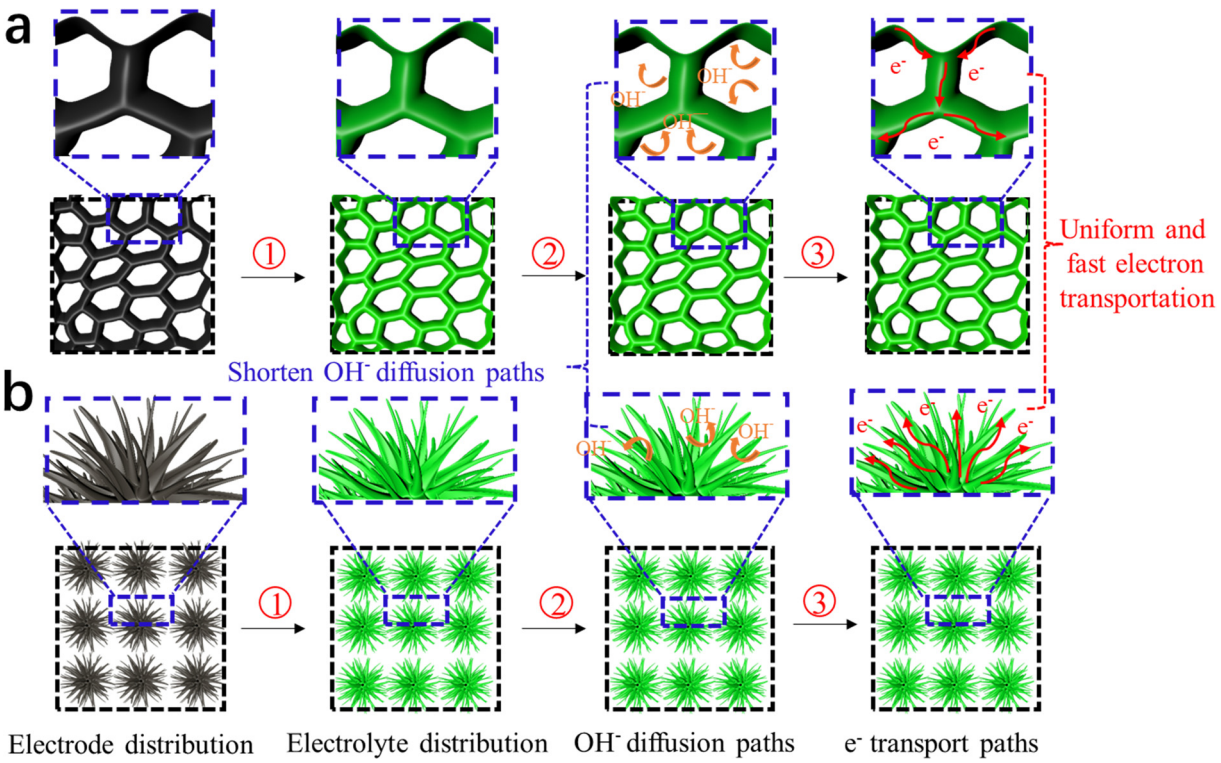

Fig. 15 Schematic illustration of the performance mechanism of DMCO. (a) Honeycomb-like $MgCo_2O_4$ and (b) urchin-like $MgCo_2O_4$.

shows the application of two tandem DMCO//AC ASCs effortlessly lighting a yellow light-emitting diode (LED) for 24 min and the variation in brightness at different times, undoubtedly indicating that the large specific surface of DMCO contributes to this result, apparently revealing its great commercial value for practical use.

Fig. 15 shows a schematic illustration of the electrochemical mechanism of DMCO, where Fig. 15a and b exhibit honeycomb-like and urchin-like $MgCo_2O_4$, respectively. In Fig. 15a, the numerous interval spaces are irregularly formed by the edge of sheets connected with each other, while the 3D structural urchins in Fig. 15b will be in total contact with OH^-. On one hand, these two unique features can effectively "filter" OH^-, which is conducive to increasing the contact area between the electrode material and OH^-, providing more redox active sites. On the other hand, it can shorten the OH^- diffusion distance, greatly reducing the Ohm resistance of the electrode. Therefore, a fast and highly reversible Faraday redox storage charge process can occur.

4. Conclusions

In summary, to improve the specific capacitance and structural stability of the active materials used for supercapacitors, we designed and successfully synthesized a dual-morphological $MgCo_2O_4$ electrode material grown on NF *via* hydrothermal reaction at 120 °C. The as-prepared dual-morphological electrode material under SEM observation included urchin-like $MgCo_2O_4$ and honeycomb-like $MgCo_2O_4$. It showed a large specific surface area of 100 m^2 g^{-1} and possessed abundant pores and interval spaces, fully allowing it to exhibit a superior specific capacitance of 1552.34 F g^{-1} at a current density of 1 A g^{-1} and low resistance, as well as first-class cycle stability of 110% retention when used as a binder-free electrode for a pseudocapacitor after 5500 cycles in 2 M KOH. These remarkable results suggest that the as-prepared electrode material can offer available paths, which are favorable for electrolyte penetration and transportation. Furthermore, the DMCO//AC ASC based on DMCO as the positive and AC as the negative electrode also had a high specific capacitance of 77.23 F g^{-1} under the condition of 1 A g^{-1} with a potential range of 1.6 V. Meanwhile, this ASC displayed a maximum energy density of 27.46 W h kg^{-1} at a power density of 825.9 W kg^{-1}, and even an energy density of 14.79 W h kg^{-1} at the power density of 10240 W kg^{-1}. Additionally, it maintained 98.8% of its original capacitance after 11 000 cycles, showing great potential for stable electrochemical performance. Therefore, we firmly believe that $MgCo_2O_4$ is an extremely promising electrode material with considerable value for market application in supercapacitors.

Conflicts of interest

There are no conflicts to declare.

Acknowledgements

This work was supported by Jianghan University school-level Program (2021yb021).

References

1 J. S. Xu, L. Wang, J. Zhang, J. H. Qian, J. Liu, Z. Q. Zhang, H. D. Zhang and X. Y. Liu, Fabrication of porous double-urchin-like $MgCo_2O_4$ hierarchical architectures for high-rate super-capacitor, *J. Alloys Compd.*, 2016, **688**, 933–938.
2 J. Zhou, Y. Huang, X. Cao, B. Ouyang, W. P. Sun, C. L. Tan, Y. Zhang, Q. L. Ma, S. Q. Liang, Q. Y. Yan and H. Zhang, Two-dimensional $NiCo_2O_4$ nanosheet-coated three-dimensional graphene networks for high-rate, long-cycle life supercapacitors, *Nanoscale*, 2015, **7**, 7035–7039.
3 R. Wang, X. Xue, W. Lu, H. W. Liu, C. Lai, K. Xi, Y. K. Che, J. Q. Liu, S. J. Guo and D. J. Yang, Tuning and understanding the phase interface of TiO_2 nanoparticles for more efficient lithum ion storage, *Nanoscale*, 2015, **7**, 12833–12838.
4 A. Laleh and A. Majid, Engineering hierarchical ultrathin $CuCo_2O_4$ nanosheets array on Ni foam by rapid electrodeposition meyhod toward high-performance binder-free supercapacitors, *Appl. Surf. Sci.*, 2018, **445**, 272–280.
5 H. W. Gao, X. H. Wang, G. H. Wang, C. Hao, S. S. Zhou and C. X. Huang, Urchin-like $MgCo_2O_4$@ppy core-shell composite grown on ni foam for a high-performance all-solid-state asymmetric supercapacitor, *Nanoscale*, 2018, **10**, 10190–10202.
6 S. K. Kaverlavani, S. E. Moosavifard and A. Bakouei, Designing graphene-wrapped nanoporous $CuCo_2O_4$ hollow spheres electrodes for high performance asymmetric supercapacitors, *J. Mater. Chem. A*, 2017, **5**, 14301–14309.
7 C. Chen, S. Wang, X. Luo, W. J. Gao, G. J. Huang, Y. Zeng and Z. H. Zhu, Reduced $ZnCo_2O_4$@$NiMoO_4{\cdot}H_2O$ heterostructure electrodes with modulating oxygrn vacancies for enhanced aqueous asymmetric, *J. Power Sources*, 2019, **409**, 112–122.
8 Y. Lu, L. Li, D. Chen and G. Z. Chen, Nanowires-assembled Co_3O_4@$NiCo_2O_4$ architectures for high performance all-solid-state asymmetric supercapacitor, *J. Mater. Chem. A*, 2017, **5**, 24981–24988.
9 S. Y. Zhao, B. Wu and Y. Gao, Synthesis and characterization of $NiCo_2O_4$ and its super capacitor properties, *Chem. Eng.*, 2016, **5**, 13–15.
10 J. R. Millr and P. Simon, Electrochemical capacitors for energy management, *Scince*, 2008, **321**, 651–652.
11 Q. F. Wu, Y. H. Zhao, J. Yu, D. L. Song, R. R. Chen, Q. Liu, R. M. Li and M. Q. Fan, Controled growth of hierarchical $FeCo_2O_4$ ultrathin nanosheets and Co_3O_4 nanowires on nickel foam for supercapacitors, *Int. J. Hydrogen Energy*, 2019, **60**, 31780–31789.
12 Y. Q. Qiao, Q. J. Sun, O. Sha, X. Y. Zhang, Y. F. Tang, T. D. Shen, L. X. Kong and W. M. Gao, Synthesis of Mn_3O_4 nano-materials via CTAB/SDS vesicle templating for high

performance supercapacitors, *Mater. Lett.*, 2017, **210**, 128–132.
13 T. F. Huang, C. H. Zhao, R. J. Zheng, Y. Zhao and Z. B. Hu, Facilely synthesized porous $ZnCo_2O_4$ rodlike nanostructure for high-rate supercapacitors, *Ionics*, 2015, **21**, 3109–3115.
14 S. B. Wang, J. Pu, Y. Tong, Y. Y. Chen, Y. Gao and Z. H. Wang, $ZnCo_2O_4$ nanowire arrays grown on nickel foam for high-performance pseudocapacitors, *J. Mater. Chem. A*, 2014, **2**, 5434–5440.
15 H. Y. Chen, J. P. Wang, X. R. Han, F. Liao, Y. F. Zhang, L. Gao and C. J. Xu, Facile synthesis of mesoporous $ZnCo_2O_4$ hierarchical microspheres and their excellent supercapacitor performance, *Ceram. Int.*, 2019, **45**, 8577–8584.
16 L. X. Zheng, Y. J. Zhao, P. H. Xu, Y. L. Pan, P. J. Yang, H. E. Wang, N. Li, Y. W. Shi and H. J. Zheng, Copper doped CoS_x@$Co(OH)_2$ hierarchical mesoporous nanosheet arrays as binder-free electrodes for superior supercapacitors, *J. Alloys Compd.*, 2022, **911**, 165115.
17 J. Ren, M. Shen, Z. L. Li, C. M. Yang, Y. Liang, H. E. Wang, J. H. Li, N. Li and D. Qian, Towards high-performance all-solid-state asymmetric supercapacitors: A hierarchical doughnut-like Ni_3S_2@ppy core-shell heterostructure on nickel foam electrode and density functional theory calculations, *J. Power Sources*, 2021, **501**, 230003.
18 C. X. Miao, C. L. Zhao, H. E. Wang, K. Zhu, K. Ye, Q. Wang, J. Yan, D. X. Cao, N. Li and G. L. Wang, Hollow Co-Mo-Se nanosheet arrays derived from metal-organic framework for high-performance supercapacitors, *J. Power Sources*, 2021, **490**, 229532.
19 P. Wang, X. Ding, R. Zhe, T. Zhu, C. Qing, Y. Liu and H. E. Wang, Synchronous defect and interface engineering of $NiMoO_4$ nanowire arrays for high-performance supercapacitors, *Nanomater*, 2022, **7**, 1094.
20 G. B. Pour, L. F. Aval and M. Mirzaee, CNTs supercapacitor based on the PVDF/PVA gel electrolytes, *Recent Pat. Nanotechnol.*, 2020, **2**, 163–170.
21 C. J. Zhang, H. Li, A. M. Huang, Q. Zhang, K. Rui, H. J. Lin, G. Z. Sun, J. X. Zhu, H. S. Peng and W. Huang, Rational design of a flexible CNTs@PDMS film patterned by bioinspired templates as a strain sensor and supercapacitor, *Small*, 2019, **18**, 1805493.
22 S. Q. Lin, J. Tang, K. Zhang, T. S. Suzuki, Q. S. Wei, M. K. Mukaida, Y. C. Zhang, H. Mamiya, X. L. Yu and L. C. Qin, High-rate supercapacitor using magnetically aligned graphene, *J. Power Sources*, 2021, **482**, 228995.
23 Y. Kumar, S. Chopra, A. Gupta, Y. Kumar, S. J. Uke and S. P. Mardikar, Low temperature synthesis of MnO_2 nanostructures for supercapacitor application, *Mater. Sci. Energy Technol.*, 2020, **3**, 556–574.
24 F. Raza, X. P. Ni, J. Q. Wang, S. F. Liu, Z. Jiang, C. L. Liu, H. F. Chen, A. Farooq and A. Ju, Ultrathin honeycomb-like MnO_2 on hollow carbon nanofiber networks as binder-free electrode for flexible symmetric all-solid-state supercapacitors, *J. Energy Storage Convers.*, 2020, **30**, 101467.
25 S. G. Krishnan, M. V. Reddy, M. Harilal, B. Vidyadharan, I. I. Misnon, M. Hasbi, A. Rahim, J. Ismail and R. Jose, Characterization of $MgCo_2O_4$ as an electrode for high performance supercapacitor, *Electrochim.*, 2015, **161**, 312–321.
26 V. Venkatachalam, A. Alsalme, A. Alswieleh and R. Jayavel, Double hydroxide mediated synthesis of nanostructured $ZnCo_2O_4$ as high performance electrode material for supercapacitor applications, *Chem. Eng. J.*, 2017, **321**, 474–483.
27 S. M. Chen, S. Q. Cui, S. Chandrasekaran, C. Ke, Z. F. Li, P. H. Chen, C. H. Zhang and Y. D. Jiang, Growth of $CuCo_2O_4$@$MnMoO_4$ core/shell nanosheet arrays for high energy density asymmetric supercapacitors, *Electrochim.*, 2020, **341**, 135893.
28 F. G. Ji, X. X. Pan, J. H. Qin, X. M. Chen and Q. B. Zha, Facile Synthesis of $NiMoO_4$ Nanorod Electrode for Aqueous Hybrid Supercapacitor with High Energy Density, *J. Electron. Mater.*, 2020, **49**, 4010–4017.
29 Y. F. Teng, D. Y. Yu, Y. D. Li, Y. N. Meng, Y. P. Wu, Y. Feng, Y. J. Hua, C. T. Wang, X. D. Zhao and X. Y. Liu, Facile synthesis of hierarchical $MgCo_2O_4$@MnO_2 core-shell nanosheet on nickel foam as an advanced electrode for asymmetric suercapacitors, *J. Electrochem. Soc.*, 2020, **167**, 020510.
30 X. F. Guan, P. H. Luo, X. Y. Li, Y. L. Yu, Y. J. Wang, L. Zhuo and D. G. Chen, Magnesium cobaltate nanowires@magnanese dioxide nanoflakes core-Shell arrays on graphene-decorated nickel foam for high-performance supercapacitors, *Int. J. Electrochem. Sci.*, 2018, **13**, 5016–5036.
31 Y. Wang, X. Y. Ma, S. S. Li, J. L. Sun, Y. F. Zhang, H. Y. Chen and C. J. Xu, Facile solvothermal synthesis of novel $MgCo_2O_4$ twinned-hemispheres for high performance asymmetric supercapacitors, *J. Alloys Compd.*, 2020, **818**, 152905.
32 Y. Wang, J. L. Sun, S. S. Li, Y. F. Zhang, C. J. Xu and H. Y. Chen, Hydrothermal synthesis of flower-like $MgCo_2O_4$ porous microstructures as high-performance electrode material for asymmetric supercapacitor, *J. Alloys Compd.*, 2020, **824**, 153939.
33 H. Y. Chen, X. M. Du, R. Z. Wu, Y. Wang, J. L. Sun, Y. L. Zhang and C. J. Xu, facile hydrothermal synthesis of porous $MgCo_2O_4$ nanoflakes as an electrode material for high-performance asymmetric supercapacitors, *Nanoscale Adv.*, 2020, **2**, 3263–3275.
34 Y. F. Teng, Y. D. Li, Z. Q. Zhang, D. Y. Yu, Y. Feng, Y. N. Meng, W. M. Meng, Y. P. Wu, X. D. Zhao and X. Y. Liu, One-step controllable synthesis of mesoporous $MgCo_2O_4$ nanosheet arrays with ethanol on nickel foam as an advanced electrode material for high performance suercapacitors, *Chem. – Eur. J.*, 2018, **24**, 14982–14988.
35 Y. N. Meng, D. Y. Yu and Y. F. Teng., Coating of the NiMoO4 nanosheets on different-morphology ZnCo2O4 nanoarrays on Ni foam and their application in battery-supercapacitor hybrid devices, *J. Energy Storage Convers.*, 2020, **29**, 101195.
36 Y. Chen, Y. F. Li, Z. Y. Hai, Y. K. Li, S. H. Kan, J. M. Chen, X. Chen, S. Zhuiykov, D. F. Cui and C. Y. Xue, Facile-synthesized $NiCo_2O_4$@$MnMoO_4$ with novel and functional structure for superior performance supercapacitors, *Appl. Surf. Sci.*, 2018, **452**, 413–422.
37 S. G. Krishnan, M. Harilal, I. I. Misnon, M. V. Reddy, S. Adams and R. Jose, Effect of processing parameters on

the charge storage properties of $MgCo_2O_4$ electrodes, *Ceram. Int.*, 2017, **43**, 12270–12279.

38 J. S. Corneile, J. W. He and D. W. Goodman., XPS characterization of ultra-thin MgO films on a Mo (100) surface, *Surf. Sci.*, 1994, **306**, 118–124.

39 M. Silambarasan, P. S. Ramesh, D. Geetha and V. Venkatachalam, A report on 1D $MgCo_2O_4$ with enhanced structural, morphological and electrochemical properties, *J. Mater. Sci.: Mater. Electron.*, 2017, **28**, 6880–6888.

40 S. Vijayakumar, S. Naganmuthu and K. S. Ryu, In-situ preparation of $MgCo_2O_4$ nanosheets on Ni-foam as binder-free electrode for high performance hybrid supercappacitors, *Dalton Trans.*, 2018, **47**, 6722–6728.

41 Z. Chen, V. Augustyn, X. Jai, Q. F. Xiao, B. Dunn and Y. F. Lu, High-performance sodium-ion pseudocapacitors based on hierarchically porous nanowire composites, *ACS Nano*, 2012, **6**, 4319–4327.

42 D. L. Chao, P. Liang, Z. Chen, L. Y. Bai, H. Shen, X. X. Liu, X. H. Xiao, Y. L. Zhao, S. V. Sovilov, J. Y. Lin and Z. X. Shen, Pseudocapacitive Na-ion storage boosts high-rate and areal capacity of self-branched 2D layered metal chalcogenide nanoarrays, *ACS Nano*, 2016, **10**, 10211–10219.

43 X. H. Xia, D. L. Chao, Y. Q. Zhang, J. Y. Zhan, Y. Zhong, X. L. Wang, Y. D. Wang, Z. X. Shen, J. P. Tu and H. J. Fan, Generic synthesis of carbon nanotube branches on metal oxide arrays exhibiting stable high-rate and long-cycle sodium-ion storage, *Small*, 2016, **12**, 3048–3058.

44 T. Brezesinski, J. Wang, S. H. Tolbert and B. Dunn, Ordered mesoporous α-MoO_3 with iso-oriented nanocrystalline walls for thin-film pseudocapacitors, *Nat. Mater.*, 2010, **9**, 146–151.

45 J. S. Xu, L. Wang, Y. D. Sun, J. Zhang, C. Zhang and M. Z. Zhang, Fabrication of porous $MgCo_2O_4$ nanoneedle arrays/Ni foam as an advanced electrode material for asymmetric supercapacitors, *J. Alloys Compd.*, 2019, **779**, 100–107.

46 J. Zhang, J. P. Cheng, M. Li, L. Liu, F. Liu and X. B. Zhang, Flower-like nickel-cobalt binary hydroxides with high specific capacitance: Tuning the composition and asymmetric capacitor application, *J. Electroanal. Chem.*, 2015, **743**, 38–45.

47 L. F. Cui, L. H. Huang, M. Ji, Y. G. Wang, H. C. Shi, Y. H. Zuo and S. F. Kang, High-performance $MgCo_2O_4$ nanocone arrays grown on three-dimensional nickel foams: preparation and application as binder-free electrode for pseudo-supercapacitor, *J. Power Sources*, 2016, **333**, 118–124.

48 V. Venkatachalam, A. Alsalme, A. Alswieleh and R. Jayavel, Double hydroxide mediated synthesis of nanostructured $ZnCo_2O_4$ as high performance electrode material for supercapacitor applications, *Chem. Eng. J.*, 2017, **321**, 474–483.

49 H. W. Gao, X. H. Wang, G. H. Wang, C. Hao, C. X. Huang and C. L. Jiang, Facile construction of a $MgCo_2O_4$@$NiMoO_4$/NF core-shell nanocomposite for high-performance asymmetric supercapacitors, *J. Mater. Chem. C*, 2019, **7**, 13267–13278.

50 C. L. Zhao, J. K. Zhu, Y. Q. Jiang, F. Gao, L. Xie and L. Y. Chen, Facile synthesis of spinel $MgCo_2O_4$ nanosheets for high-performance asymmetric supercapacitors, *Mater. Lett.*, 2020, **271**, 127799.

51 Z. Q. Liu, Y. Liu and Y. X. Zhong, *et al.*, Facile construction of $MgCo_2O_4$@CoFe layered double hydroxide core-shell nanocomposites on nickel foam for high-performance asymmetric supercapacitors, *J. Power Sources*, 2021, **484**, 229288.

52 Z. Q. Liu, A. H. Li and Y. L. Qiu, *et al.*, $MgCo_2O_4$@NiMn layered double hydroxide core-shell nanocomposites on nickel foam as superior electrode for all-solid-state asymmetric supercapacitors, *J. Colloid Interface Sci.*, 2021, **592**, 455–467.

53 R. Z. Wu, J. L. Sun and X. Y. Ma, *et al.*, Uniform $MgCo_2O_4$ porous nanoflakes and nanowires with superior electrochemical performance for asymmetric supercapacitors, *J. Alloys Compd.*, 2021, **884**, 161087.

54 Z. Q. Liu, Y. X. Zhong and Y. L. Qiu, *et al.*, Multilayered and hierarchical structured NiCo double hydroxide nanosheets generated on porous $MgCo_2O_4$ nanowire arrays for high performance supercapacitors, *Appl. Surf. Sci.*, 2021, **546**, 149133.

55 J. J. Fu, L. Li, J. M. Yun, D. M. Lee, B. K. Ryu and K. H. Kim, Two-dimensional titanium carbide (MXene)-wrapped sisal-like $NiCo_2S_4$ as positive electrode for high-performance hybrid pouch-type asymmetric supercapacitor, *Chem. Eng. J.*, 2019, **375**, 121939.

56 S. X. Zhou, H. L. Fan, F. He, Z. B. Fu, G. M. Gao, S. Zhang and X. Hu, Role of selenium on the pseudocapacitance of nickel-cobalt selenide, *J. Energy Storage*, 2022, **52**, 104832.

57 Y. Zhang, H. Liu, M. Huang, J. M. Zhang, W. Zhang, F. Dong and Y. X. Zhang, Engineering Ultrathin $Co(OH)_2$ Nanosheets on Dandelion–like $CuCo_2O_4$ Microspheres for Binder-Free Supercapacitors, *ChemElectroChem*, 2017, **4**, 721–727.

58 Y. Zhou, L. Ma, M. Y. Gan, M. H. Ye, X. R. Li, Y. F. Zhai, F. B. Yan and F. F. Cao, Monodisperse MnO_2@$NiCo_2O_4$ core/shell nanospheres with highly opened structures as electrode materials for good-performance supercapacitors, *Appl. Surf. Sci.*, 2018, **444**, 1–9.

59 J. Y. Wang, S. Sarwar, J. Song, L. J. Du, T. B. Li, Y. D. Zhang, B. B. Li, Q. Q. Guo, J. J. Luo and X. Y. Zhang, One-step microwave synthesis of self-supported $CoSe_2$@ $NiSe_2$ nanoflowers on 3D nickel foam for high performance supercapacitors, *J. Alloys Compd.*, 2022, **892**, 162079.

60 Y. Y. Zheng, Y. R. Tian, S. Sarwar, J. J. Luo and X. Y. Zhang, Carbon nanotubes decorated $NiSe_2$ nanosheets for high-performance supercapacitors, *J. Power Sources*, 2020, **452**, 227793.

61 Y. L. Yuan, W. C. Wang, J. Yang, H. C. Tang, Z. Z. Ye, Y. J. Zeng and J. G. Lu, Three-dimensional $NiCo_2O_4$@Mn-MoO_4 core-shell nanoarrays for high-performance asymmetric supercapacitors, *ACS*, 2017, **40**, 10446–10454.

62 P. Zhang, H. He and Q. Li, Ni–Co–S nanosheets supported by $CuCo_2O_4$ nanowires for ultra-high capacitance hybrid supercapacitor electrode, *Int. J. Hydrogen Energy*, 2020, **45**, 4784–4792.

63 M. Li, Z. Y. Meng, R. C. Feng, K. L. Zhu, F. F. Zhao, C. R. Wang, J. L. Wang and P. K. Chu, F, Fabrication of Bimetallic Oxides (MCo_2O_4: M = Cu, Mn) on Ordered Microchannel Electro-Conductive Plate for High-Performance Hybrid Supercapacitors, *Sustainability*, 2021, **17**, 9896.